Elastic-Plastic-Failure Finite Element Analyses of Railroad Tank Car Heads in Impact

Hailing Yu[1], Yim H. Tang[2], and David Y. Jeong[2]

[1] Chenega Advanced Solutions & Engineering, LLC, Cambridge, MA 02142, USA

[2] Volpe National Transportation Systems Center, Cambridge, MA 02142, USA

Abstract: This paper presents a computational framework that employs elastic-plastic-failure finite element analysis (FEA) tools to predict dynamic forces, deformations and puncture resistance of railroad tank car heads in impact events. First, computational sensitivity to analysis code, analysis type, element type, element size, through-the-thickness characteristics and element integration scheme is studied for elastic-plastic analyses. The fully integrated shell element formulation in ABAQUS/Explicit yields acceptable global impact force-indentation responses in dynamic analyses, and the results converge with 3-4 through-the-thickness Gaussian integration points and a characteristic element size 1-2 times the tank thickness. Second, the progressive damage and failure modeling for ductile metals is employed to estimate the puncture resistance of a tank car head. The Bao-Wierzbicki fracture initiation criterion expressed in the stress triaxiality-equivalent plastic strain plane is employed to predict damage initiation in the tank car material. The maximum impact force F_{max} *predicted from dynamic puncture analyses shows mesh dependence and decreases as the mesh refines.* F_{max} *with infinitesimal mesh refinement is then extrapolated from a regression analysis of* F_{max} *obtained with finite meshes, and it is designated as the puncture force or the impact force at which puncture of a tank head is expected to occur. The puncture energy and puncture velocities are further calculated based on the estimated puncture force and the assumptions of conserved energy and momentum. The FEA framework is applied to selected cases from an existing experimental study of tank car heads, and key results compare favorably with those from alternative methods.*

Keywords: Railroad Tank Car Head, Impact, Elastic-Plastic FEA, Failure FEA, Fracture Initiation Criterion, Mesh Dependence, Puncture Resistance, Puncture Force, Puncture Velocity.

1. Introduction

Tank cars are commonly used in railroad industry to transport liquefied goods. Specialized tank cars are designed to carry hazardous materials such as compressed flammable (e.g., propane) or toxic gases (e.g., chlorine). The risk of tank car puncture and subsequent release of harmful substances in an impact event involving these tank cars is of great concern to the railway industry and transportation safety agencies. In a series of derailment and/or collision accidents in recent years, impact loading on a tank car caused fracture or puncture of the tank car structure, and subsequent releases of hazardous materials led to human injuries/fatalities, economic losses and environmental degradation (NTSB, 2004, 2005 and 2006). These accidents renewed a call for detailed studies of the structural integrity of tank cars involved in accidents, and specifically a better understanding of the puncture resistance of a tank car subjected to dynamic impact loading is needed. While there is no indication that the puncture risk associated with a shell (i.e., the cylindrical mid-body) is lesser than that associated with a head (i.e., one of the two ellipsoidal ends), this paper deals with a tank car head and its puncture resistance prediction as a first phase in an ongoing study.

Previous experimental studies included reduced- and full-scale impact tests conducted on the heads of a number of steel (Phillips and Olsen, 1972; Coltman and Hazel, 1992) or aluminum tank cars (Larson, 1992). Full-scale tests were designed to hint on the puncture velocity, or the minimum impact velocity at which puncture of a tank head was expected to occur. In such a test, a coupler attached to a ram car driven by an initial velocity struck a full-scale tank head. As a result, the head was deformed with a dent (in which case the maximum impact force and dent sizes were recorded) or punctured (in which case the initial impact velocity indicated an upper bound for the puncture velocity). Full-scale tests were expensive to conduct and yet very important to validate an analytical or computational study.

There were a few studies that employed analytical or computational methods to predict the puncture resistance of tank cars. To predict the local failure of a metal tank car structure, a fracture initiation criterion was needed. Stahl (2000) used a strain-based criterion that would stop the impact simulation of a tank head/shell once the maximum principal engineering strain in the domain reached an ultimate strain parameter obtained from uniaxial tensile tests on the same material – the percent elongation in 2 inches. The area under the force-indentation curve obtained from the analysis was then calculated as the energy needed to initiate puncture. Jeong et al. (2001a,b and 2006) adopted a semi-empirical, semi-analytical approach to predict the puncture forces and velocities of tank car heads and compared the results with available experimental data. In this approach, a shear stress criterion was applied and puncture was believed to occur once the calculated maximum shear stress reached the ultimate shear strength. The more recent paper also explored the application of finite element analysis (FEA) tools in tank car studies (Jeong et al., 2006).

In this paper, an elastic-plastic-failure FEA framework was developed, and strain based, stress triaxiality dependent fracture initiation criteria for ductile metals were applied in ABAQUS to predict the puncture resistance of a tank car head. Six impact test cases were identified from the RPI-AAR tank car head study (Phillips and Olsen, 1972), and Table 1 presents the information of these tests and the puncture forces and velocities estimated from the semi-empirical approach (Jeong et al., 2001a,b and 2006). In all six cases, the total ram car weight is W_{ram}=128.9 kips and the tank car material is AAR M-115 (or M-115) steel. The aspect ratio of the oblate spheroidal head shape is 2:1. All impacts occurred at the head center except for those noted otherwise. Selected cases from Table 1 without fluids (or having 100% outage) were simulated and demonstrated in the elastic-plastic-failure FEA framework. The paper is organized as follows: elastic-plastic FEA including the definition of a model problem, sensitivity studies and case studies compared with test data and/or semi-empirical results, introduction of the failure FEA framework for puncture resistance analyses including a review of the progressive damage and failure modeling in ABAQUS/Explicit, calibration of fracture initiation and strain softening parameters and puncture resistance estimation, application of the failure FEA framework in case studies, and discussion and conclusions.

Table 1. Test information and puncture forces/velocities estimated from the semi-empirical approach for six test cases identified from the RPI-AAR tank head study.

Case	Impact series/No.	D (inch.)	t (inch.)	W_{tank} (kips)	Backup cars	Outage	$F_{p,SE}$ (kips)	$v_{p,SE}$ (mph)
1	First/1-3	78.0	0.5	96.6	0	2%	411.5	17.9
2[a]	Second/1-2	87.5	0.5	48.5	0	100%	461.6	20.1
3	First/4-5	80.0	0.4375	107.3	0	2%	369.3	16.5
4[b]	First/25	88.0	0.4375	48.0	3	100%	406.2	18.5
5	First/20-21	83.0	0.4375	40.9	3	100%	383.2	18.0
6	First/6	88.0	0.4375	128.9	0	2%	406.2	17.4

[a] Impacted 1/3 down from head center.
[b] Impacted at knuckle near the bottom of the head.
Symbols:
D tank car inner diameter
t tank car thickness
W_{tank} tank car weight including fluid but excluding backup cars, if any
$F_{p,SE}$ puncture force estimated from the semi-empirical approach
$v_{p,SE}$ puncture velocity estimated from the semi-empirical approach

2. Elastic-plastic analyses

Tank car heads with considerable plastic deformations but free of any fracture or puncture were first studied in the elastic-plastic FEA. A model problem was extracted from a case in Table 1 and extensive sensitivity studies were conducted on this problem. Acceptable modeling setup was then applied to typical cases in Table 1 and the results compared with those obtained from alternative methods.

2.1 Model problem definition

Case No.5 of Table 1 was selected as the model problem. The following simplifications or assumptions were made: the tank car body other than the head being impacted was not modeled; a fixed boundary condition was applied along the circular edge of the head; the backup cars were not modeled; the ram car was modeled as a rigid body having a generic box shape with a distributed mass; the impactor in front of the ram car was a digitally processed coupler whose scanned images were obtained in a post-accident analysis; and quarter symmetry was assumed. Strictly speaking, the unsymmetrical shape of the coupler did not warrant quarter symmetry, but it was assumed for simplicity and without compromising the objective of the analyses.

Figure 1(a) shows a full view of the dynamic simulation setup for the model problem, and Figure 1(b) shows a zoomed view of the impact zone. About 23.29 sq. in. area of the coupler was in contact with the head (i.e., an equivalent 93 sq. in. contact area for the full model). The coefficient of kinetic friction between the coupler and the tank head was assumed to be 0.57. The impact velocity was set at a moderate 8.5 mph for the problem to remain elastic-plastic. Similarly, static simulations were conducted on the same tank head (Figure 2). The boundary conditions were the same as those in the dynamic simulations. A traction load was applied over a quarterly circular area in the head center. The loaded area was set to 23.29 sq. in. in the quarter model.

The following elastic-plastic material properties were adopted for modeling the M-115 steel: Young's modulus E=30,000 ksi, Poisson's ratio ν=0.3, yield strength σ_Y=30 ksi, and Ramberg-Osgood strain hardening law,

$$\varepsilon = \sigma/E + (\sigma/K)^n \tag{1}$$

where ε and σ are true strain and true stress, respectively, and n=6.65, K=73.1 ksi.

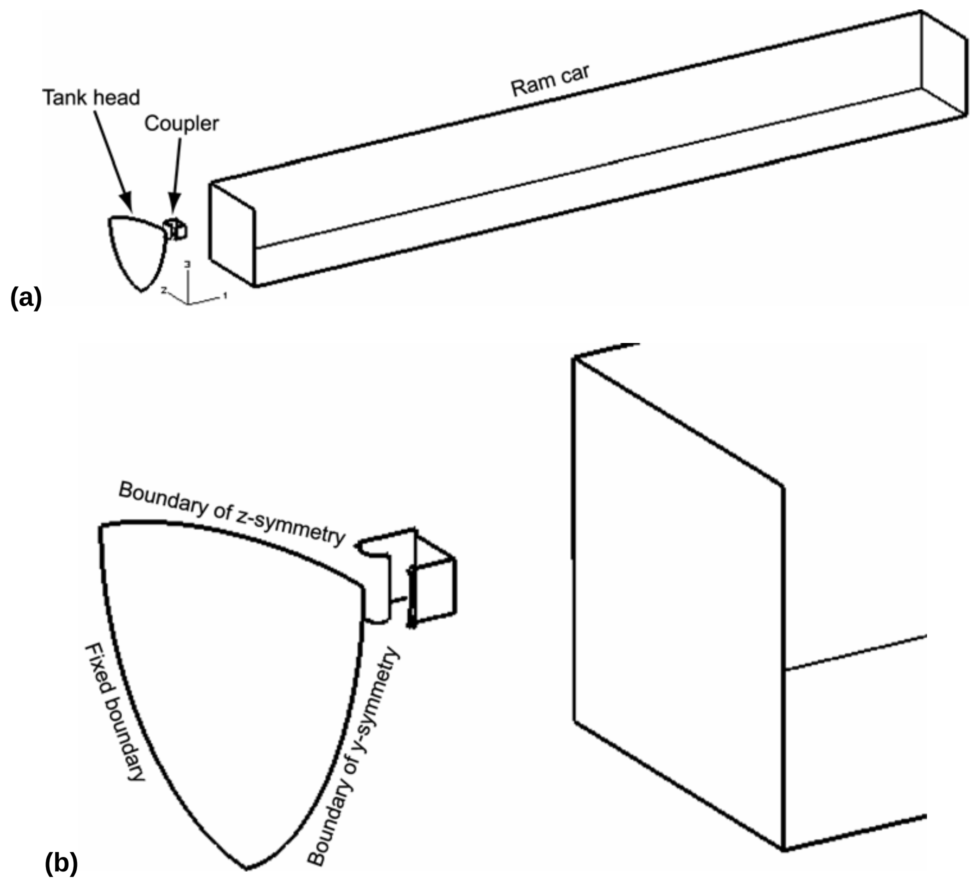

Figure 1. Dynamic simulation setup for the model problem with quarter symmetry: (a) full view, and (b) zoomed view of the impact zone.

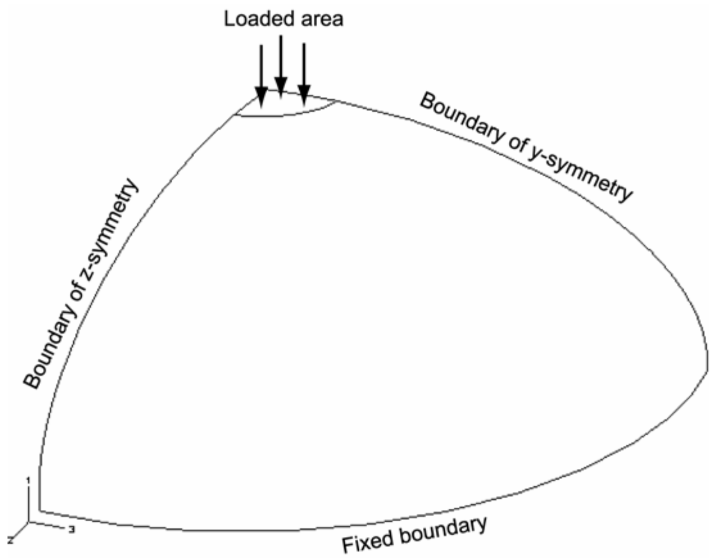

Figure 2. Static simulation setup for the model problem with quarter symmetry.

The main result of interest from a dynamic or a static analysis was the impact force-indentation (*F-d*) response. The force was derived from the contact force output (dynamic) or as the resultant of the traction load (static). The indentation was averaged displacements over the loaded area in a static analysis and the dent depth in a dynamic analysis. The simulation time of a dynamic analysis was set to 0.35 seconds for a complete *F-d* curve to be obtained.

2.2 Sensitivity studies

Both software ABAQUS and LS-Dyna were employed (ABAQUS, 2006a; LSTC, 2003). The LS-Dyna version was 970. The ABAQUS version was a prerelease 6.6-PF1with fully integrated elements available in the explicit code. Static analyses were conducted using ABAQUS/Standard only. The sensitivity studies were aimed at answering the following questions: (1) Are ABAQUS and LS-Dyna results comparable? (2) What are the acceptable element sizes and numbers of through-the-thickness integration points for shell elements? (3) What are the acceptable aspect ratios and through-the-thickness layers for solid elements? (4) How are dynamic results compared with static results? (5) Solid and shell elements: is one type preferred over the other? (6) Are solutions from reduced integration elements acceptable?

The last question was answered first. Single integration point elements with various hourglass control techniques were investigated. Although similar global *F-d* curves could be achieved with some types of hourglass control, strain distributions in these cases were often inconsistent. The "enhanced" hourglass control in ABAQUS/Explicit could result in reasonable strain distributions, but the resulting *F-d* curves were much stiffer. Thus it was determined that reduced integration elements were not suitable for this study.

Dynamic analyses were conducted using ABAQUS/Explicit and/or LS-Dyna. Figure 3(a) shows the dynamic analysis results from both programs using two solid meshes: 1:1 aspect ratio and 1 layer of through-the-thickness elements, and 2:1 aspect ratio and 2 layers of through-the-thickness elements. Figure 3(b) shows the dynamic analysis results using shell meshes with a characteristic element size a=1t and 3-4 through-the-thickness integration points. Note shell element formulation No. 16 was selected for LS-Dyna analyses, and Gaussian integration type was selected for ABAQUS shell elements. The two programs yielded nearly indistinguishable results in the solid element cases. In the shell element cases, ABAQUS and LS-Dyna results are very close up to an indentation level of about 17 inches, beyond which the LS-Dyna results appear to be more compliant, with lower maximum forces (F_{max}) and higher maximum/residual indentations (d_{max}/d_{res}) than the ABAQUS results. The differences in F_{max}, d_{max} and d_{res} are within 6% between the two programs.

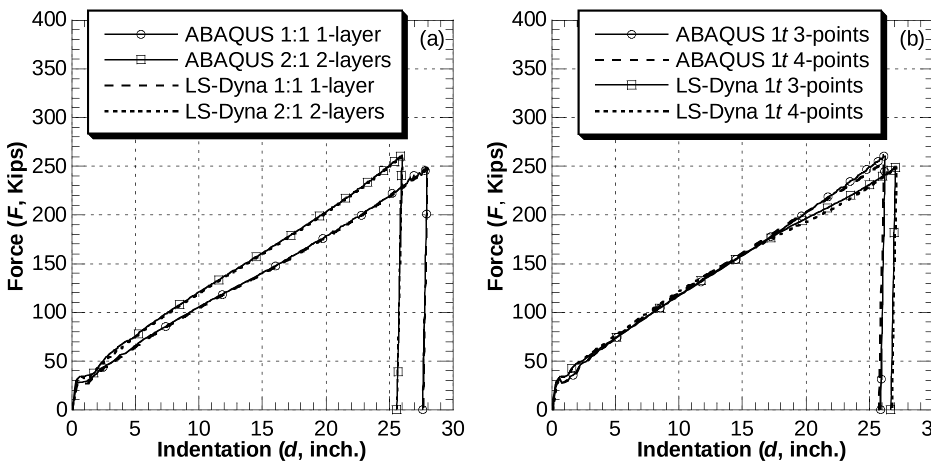

Figure 3. Comparison of force-indentation (*F-d*) curves obtained from ABAQUS/Explicit and LS-Dyna using (a) solid elements, and (b) shell elements.

Figures 4(a-b) compare static analysis results obtained using shell elements with (a) 2-5 through-the-thickness integration points with a=1t, and (b) a=1t and 0.5t with 3 through-the-thickness integration points. Figures 4(c-d) show the same comparisons for the dynamic results (with an additional case of a=2t in Figure 4d). Judged from these global *F-d* plots, convergence seems to be achieved with 3-4 through-the-thickness integration points and a=1t or 2t.

Figure 5 compares the solid element results obtained with different mesh characteristics. With an element aspect ratio 1:1, the characteristic element size a=t/2 for 2 layers of elements and a=t/3 for 3 layers of elements. In the static case shown in Figure 5(a), the curve corresponding to 3 layers of elements is incomplete owing to an interrupted long simulation. The available results for 2 and 3 layers of elements are nearly identical, indicating convergence is achieved with a=t/2. The same is true for the dynamic analysis results (Figure 5b). It is noted that in Figure 5(b), a 2:1 element aspect ratio yields the stiffest *F-d* responses, which may be explained by shear locking associated with poorer element aspect ratios (LSTC, 2003).

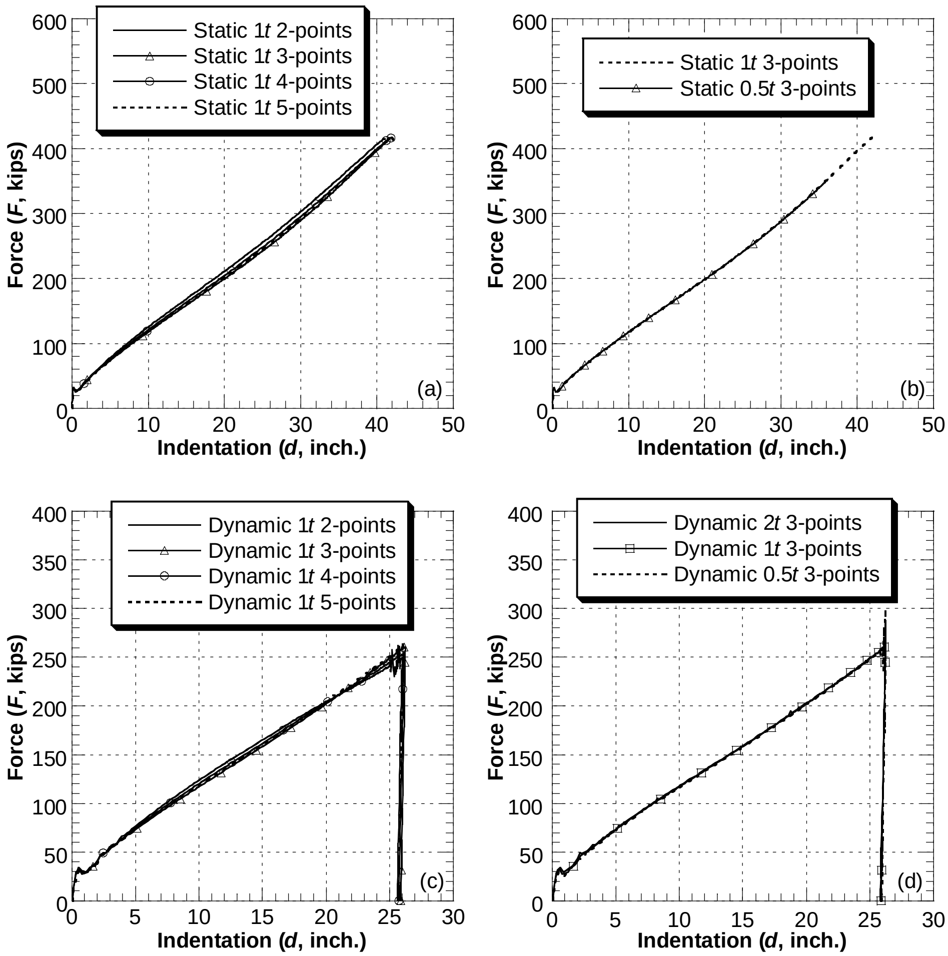

Figure 4. Comparison of force-indentation (*F-d*) curves obtained using shell elements from (a) static analyses with 2-5 through-the-thickness integration points, (b) static analyses with 1*t* and 0.5*t* element sizes, (c) dynamic analyses with 2-5 through-the-thickness integration points, and (d) dynamic analyses with 2*t*, 1*t* and 0.5*t* element sizes.

Figure 6 compares the *F-d* curves obtained from static and dynamic analyses. Figure 6(a) shows the solid element results with 2 layers of elements and 1:1 element aspect ratio. Figure 6(b) shows the shell element results with a=1t and 3 through-the-thickness integration points, and the dynamic results from both ABAQUS and LS-Dyna are shown. In the ABAQUS shell element case, dynamic responses are equally stiff or stiffer than static responses, but the solid element case displays a different trend, i.e., the static responses are mostly stiffer than the dynamic responses. In Figure 6(b), as pointed out previously, starting at an indentation level of about 17 inches, the *F*-

d curve from an LS-Dyna shell analysis deviates from and becomes more compliant than the corresponding ABAQUS curve as well as the static curve.

Finally, Figure 7 compares the *F*-*d* responses obtained from typical solid and shell element analyses. The static results obtained using both element types are almost identical (Figure 7a). As to the dynamic results in Figure 7(b), the solid element response appears to be more compliant than the ABAQUS shell analysis result, and the LS-Dyna shell curve first joins the ABAQUS shell curve and later transitions to join the solid element curve.

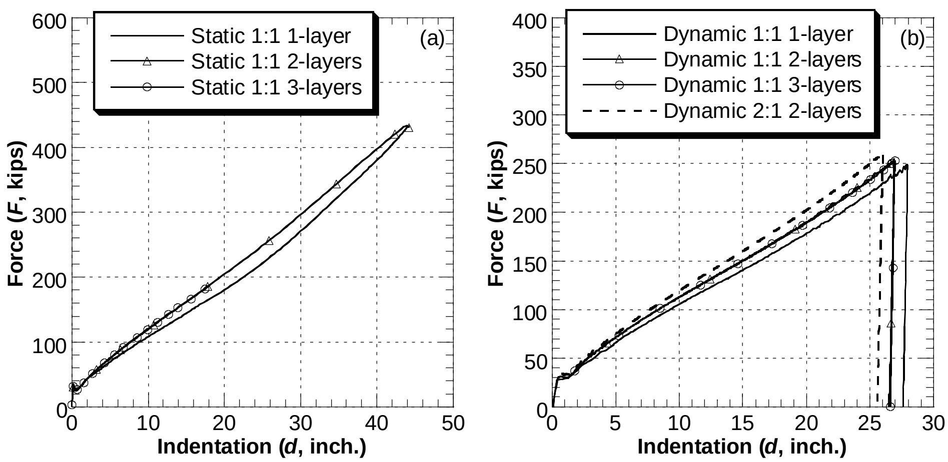

Figure 5. Comparison of force-indentation (*F-d*) curves obtained from (a) static, and (b) dynamic analyses using solid elements.

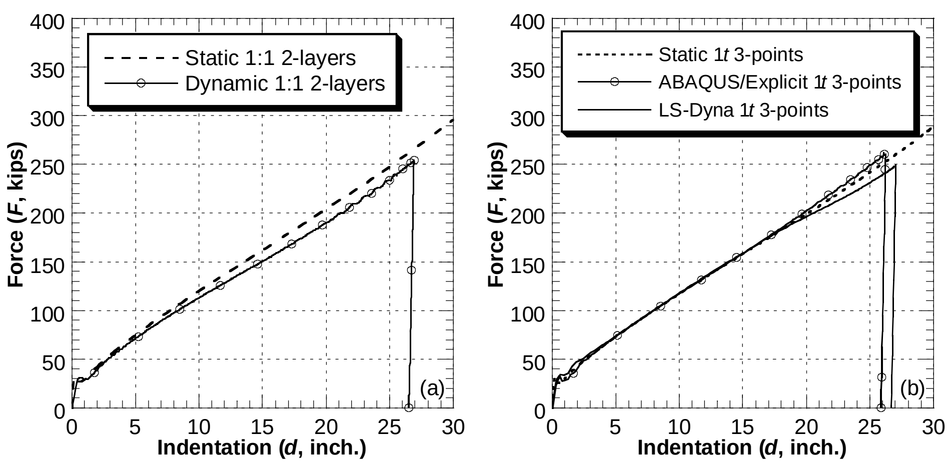

Figure 6. Comparison of force-indentation (*F-d*) curves obtained from static and dynamic analyses using (a) solid elements, and (b) shell elements.

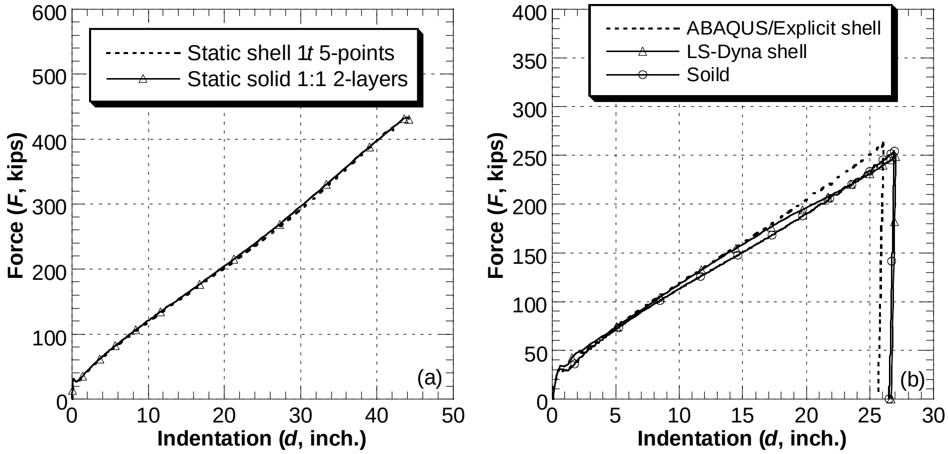

Figure 7. Comparison of force-indentation (*F-d*) curves obtained using shell and solid elements from (a) static, and (b) dynamic analyses.

2.3 Case studies

A quick case study was to examine Case No. 5 of Table 1 on which the model problem was based. There was a single *F-d* data point for this case from the report (Phillips and Olsen, 1972): an impact with an initial ram velocity 8.5 mph produced a dent with d_{res}=9 inches, and the recorded F_{max} was 118 kips. In Figure 8, the data point (d_{res}, F_{max}) is plotted on the *F-d* curve obtained from the model problem FEA and appears to be in close vicinity of the FEA curve. Note a (d_{max}, F_{max}) data point would shift slightly rightward as d_{max} would be slightly larger than d_{res}. The tank car body and backup cars behind the impacted head in Case No. 5 were omitted in the model problem, and this helped to concentrate the input kinetic energy on impacting the head and consequently produced larger indentation in the model problem than in the test case.

Case No. 2 of Table 1 was simulated next. The impact was off-center with the coupler striking 1/3 down from the head center, so half symmetry models were developed. There were no backup cars. In dynamic analyses, the tank car body behind the head being struck was modeled as a rigid body. The tank body length excluding both heads was estimated to be 363.28 inches from the volumetric data of the tank car. Two lumped masses, each weighing 8.02 kips in half symmetry, were assigned at the bottom of the two heads to make up the correct tank car mass. Gravity load was applied to the entire model, and a stationary rigid floor was employed to prevent the tank car's downward movement.

In Figure 9(a), the *F-d* curves obtained from two static analyses are presented: center loading and off-center loading resembling that in Case No. 2. The response from the off-center loading is slightly stiffer than that from the center loading. Dynamic analysis results with four initial impact velocities, i.e., v_0=5, 8.8, 15 and 20 mph, are also presented. The dynamic responses follow the static responses closely. The increase in the maximum impact force F_{max} with increased v_0 is further demonstrated in Figure 9(b). In addition to the FEA results, those from the semi-empirical study (Jeong et al., 2001a,b and 2006) and two data points from the tests (Phillips and Olsen, 1972) are also plotted in Figure 9(b). Compared to the semi-empirical study, the FEA predicted higher F_{max} at lower v_0 and lower F_{max} at higher v_0. Despite that, the predictions by the two approaches were considered comparable.

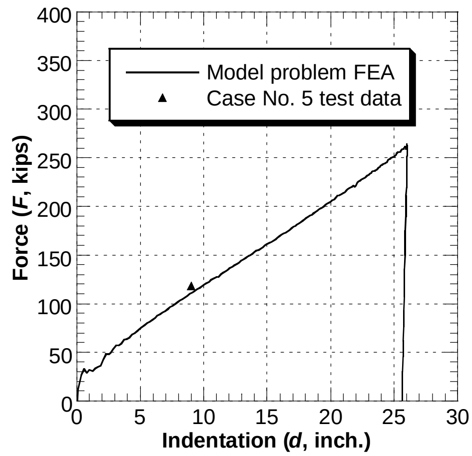

Figure 8. Comparison of the *F-d* curve obtained from the model problem FEA with the available test data for Case No. 5. The impact velocity was 8.5 mph.

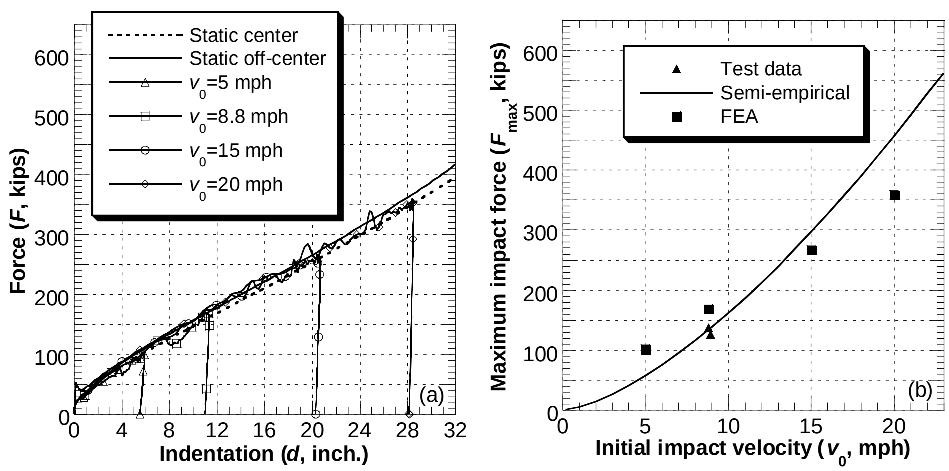

Figure 9. Case No. 2 results: (a) *F-d* responses from static and dynamic FEA with four initial impact velocities, and (b) comparison of the maximum impact force-initial impact velocity (F_{max}-v_0) relations among available test data, semi-empirical results and FEA results. SAE filter with frequency 100 was applied to the dynamic *F-d* curves owing to noisy responses around the peak forces.

3. Puncture analysis framework

As discussed, for an FEA method to predict fracture or puncture of a tank car structure, a fracture initiation criterion is needed, and an FEA program needs to be able to predict the onset of fracture according to such a criterion. ABAQUS progressive damage and failure modeling for ductile metals was identified as such a method and is briefly reviewed, followed by a discussion of the calibration of fracture initiation and strain softening parameters. The theoretical framework for predicting the puncture resistance of a tank head is then laid out.

3.1 ABAQUS progressive damage and failure modeling for ductile metals

Figure 10(a) shows a stress-strain (σ-ε) relation employed in ABAQUS/Explicit for ductile metals up to complete material failure. Typical linear elastic and strain hardening responses are followed first. As the yield stress evolves to the peak level, an additional overall damage variable D is introduced and damage initiates with D=0. The equivalent plastic strain at the onset of damage is denoted as $\bar{\varepsilon}_0^{\text{pl}}$, and it can be a function of stress triaxiality, strain rate, temperature, etc. Subsequently the yield stress softens and the elastic modulus degrades until the strain reaches $\bar{\varepsilon}_f^{\text{pl}}$, or the equivalent plastic strain at complete failure, and D reaches the maximum degradation $D_{\text{max}} \leq 1$. Finally, elements representing failed material points are removed from the model.

To deal with the spurious mesh dependence associated with strain softening or "strain localization," an element characteristic length L_e is introduced. For shell and 2-D elements, L_e is the square root of the integration point area, and for 3-D elements, it is the cubic root of the integration point volume (ABAQUS, 2006a). Then a stress-displacement (σ-u) relation shown in Figure 10(b) replaces the σ-ε relation in Figure 10(a) in the material property definitions, where u is related to ε by L_e: $u = L_e\varepsilon$. Following damage initiation, the equivalent plastic displacement $\bar{u}^{\text{pl}}$ evolves according to $\dot{\bar{u}}^{\text{pl}} = L_e\,\dot{\bar{\varepsilon}}^{\text{pl}}$ until it reaches $\bar{u}_f^{\text{pl}}$ at failure.

Damage evolution laws dictating the strain softening responses can be displacement-based or energy-based in ABAQUS/Explicit. The former requires an input of the parameter $\bar{u}_f^{\text{pl}}$, whereas the latter requires that of G_f, the fracture energy dissipated per unit area during the damage process. Because it was difficult to calibrate G_f in this study, displacement-based damage evolution laws were adopted. The softening curves can be assigned tabular, linear or exponential forms.

Some limitations exist in the progressive damage and failure modeling described above. The definition of L_e indicates that some mesh dependence is still expected when elements have poor aspect ratios. Although L_e is introduced to "counteract" the effect of strain localization, damage initiation prediction is based on a local strain quantity $\bar{\varepsilon}_0^{\text{pl}}$, which can lead to mesh sensitivity when strain concentration is present. An alternative solution could be a nonlocal numerical approach that defines material characteristic lengths L_m as additional material parameters. For instance, in nonlocal damage analyses of concrete, L_m is sometimes defined as the width of the localization band, and in strain-softening related calculations, the local strain is replaced with a weighted average strain over a representative volume determined by L_m (e.g., Pijaudier-Cabot and Bazant, 1987; Comi, 2001). In the case of concrete, L_m differs in tension and compression. It is not clear, however, if material characteristic lengths (or strain localization bands) are as significant for ductile metals as they are for quasi-brittle materials such as concrete, and nonlocal material modeling is beyond the scope of the current study.

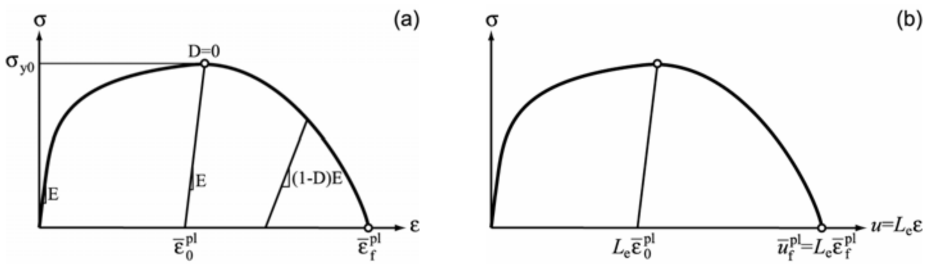

Figure 10. Illustration of ABAQUS progressive damage and failure modeling for ductile metals: (a) typical stress-strain (σ-ε) relation, and (b) stress-displacement (σ-u) relation with the introduction of an element characteristic length L_e.

3.2 Fracture initiation and strain softening calibrations

A fracture initiation criterion plotted in the stress triaxiality-equivalent plastic strain plane ($\eta, \bar{\varepsilon}_0^{pl}$) is referred to as a fracture locus. The stress triaxiality η is defined as the ratio of the hydrostatic mean stress (σ_m) to the von Mises equivalent stress ($\bar{\sigma}$):

$$\eta = \sigma_m / \bar{\sigma} \tag{2}$$

where

$$\sigma_m = (\sigma_1 + \sigma_2 + \sigma_3)/3 \tag{3}$$

$$\bar{\sigma} = \left[(\sigma_1 - \sigma_2)^2 + (\sigma_2 - \sigma_3)^2 + (\sigma_3 - \sigma_1)^2\right]^{\frac{1}{2}} \Big/ \sqrt{2} \tag{4}$$

For instance, in a uniaxial stress state, $\sigma_m=\sigma_1/3$, $\bar{\sigma}=\sigma_1$, and it follows $\eta=1/3$. Numerous analytical and experimental studies have been conducted to construct the fracture loci for aluminum and steel materials. Wierzbicki et al. (2005) compared seven fracture models by mapping all models onto the ($\eta, \bar{\varepsilon}_0^{pl}$) plane and evaluating them against experimental data. A fracture model by Hooputra et al. (2004) that treated ductile and shear fractures separately was implemented in ABAQUS/Explicit. The Bao-Wierzbicki model (Bao, 2003) also considered the transitional modes between ductile and shear factures. For industrial applications, Lee and Wierzbicki (2004) further presented a simplified version of the Bao-Wierzbicki model with a reduced number of required parameters, which could simply be calibrated from uniaxial tensile test data. This led to the adoption of the Bao-Wierzbicki fracture model in this study.

The fracture locus of aluminum or steel is believed to have three distinct branches as shown in Figure 11: Branch I is for η>1/3 and fracture due to the mechanism of void nucleation, growth and coalescence; Branch III is for negative η and shear decohesion fracture; and Branch II is for a combination of the above two modes. Further, these three branches can be approximated with the following analytical functions (Lee and Wierzbicki, 2004):

$$\bar{\varepsilon}_0^{\mathrm{pl}} = \begin{cases} \infty, & \eta \le -1/3 \\ C_1/(1+3\eta), & -1/3 < \eta \le 0 \\ C_1 + (C_2 - C_1)(\eta/\eta_0)^2, & 0 \le \eta \le \eta_0 \\ C_2\,\eta_0/\eta, & \eta_0 \le \eta \end{cases} \tag{5}$$

where C_1 is the critical fracture initiation strain in pure shear (η=0), and η_0 and C_2 are the stress triaxiality and the critical fracture initiation strain, respectively, in uniaxial tension. It is noted that the Bao-Wierzbicki fracture locus employs the concept of averaged stress triaxiality η_{ave} over the deformation history domain, but in ABAQUS damage modeling, an "instantaneous" η is more likely in use. Thus the subscript "ave" is dropped in Equation (5).

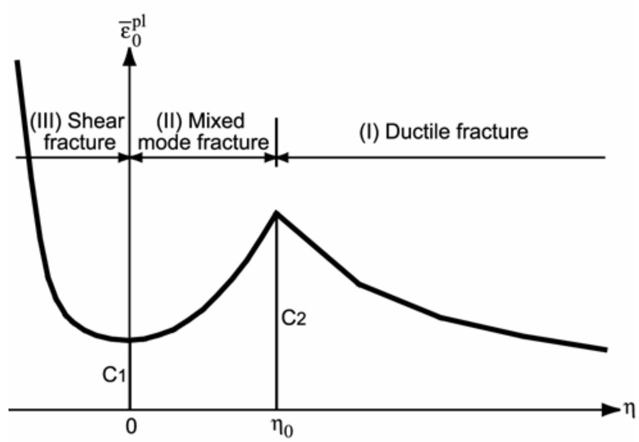

Figure 11. Typical Bao-Wierzbicki fracture locus for ductile metals.

Uniaxial tensile properties of tank car steel materials were searched in the literature, but no additional material tests were conducted. We relied on the material test reports from National Institute of Standards and Technology (NIST) to construct the fracture loci for the M-115 and the AAR TC-128 Grade B steel materials (Hicho and Harne, 1991; Zahoor, 1998). Typical uniaxial tensile test data are: 0.2% offset yield strength (σ_Y), ultimate tensile strength (σ_U), all in engineering measure, reduction in area (A_R, positive for reduction), and percent elongation (ε_E) in a given specimen length. The fracture parameters calibrated from these data for a type of M-115 steel (Specimen 06 and Test T, Zahoor, 1998) were: C_1=0.369, η_0=0.512, and C_2=1.056.

The softening curves were assigned linear forms. There was no direct measurement of the effective plastic displacement $\bar{u}_{\mathrm{f}}^{\mathrm{pl}}$. Assume that in a uniaxial tensile test, the strain localization at failure has a magnitude $\varepsilon_{1\mathrm{f}}$ that occurs in a zone with a material characteristic length L_{m}. Then the plastic displacement at failure may be determined by:

$$\bar{u}_{\mathrm{f}}^{\mathrm{pl}} = u_{1\mathrm{f}}^{\mathrm{pl}} = L_{\mathrm{m}}\varepsilon_{1\mathrm{f}} \tag{6}$$

Because the data of $\varepsilon_{1\mathrm{f}}$ and L_{m} were unavailable, they were simply replaced with ε_{E} and the specimen length over which ε_{E} was measured. For the M-115 steel considered above, $\bar{u}_{\mathrm{f}}^{\mathrm{pl}}$ was determined to be approximately 0.75 inches.

3.3 Puncture resistance prediction

Integration of the force F with respect to the indentation d from an F-d curve results in the work W done by the force. A cross plot between W and F can hint on the energy required to puncture a tank head if the puncture force, or the impact force at which puncture of a tank head is expected to occur, is determined beforehand. Assume that the puncture force of a tank head is estimated from FEA as $F_{\mathrm{p,FE}}$, then the energy required to puncture the tank head, $E_{\mathrm{p,FE}}$, may include energies dissipated in plastic deformation, damage and friction in the tank-impactor contact and be defined as the work corresponding to $F_{\mathrm{p,FE}}$, or

$$E_{\mathrm{p,FE}} = W\Big|_{F=F_{\mathrm{p,FE}}} \tag{7}$$

In the model problem case where the tank head being struck is fixed along the edge between the head and the shell, the kinetic energy gained by the tank car from impact may be ignored. The initial impact velocity of the ram car is assumed to be v_0, and its residual velocity after impact is assumed to be v, all expressed along the impact direction. With a relatively low impact momentum (which is solely determined by v_0 with a given ram mass), the ram car bounces back after impact, and v_0 and v have opposite signs. With a sufficiently large v_0, the tank head is punctured and after impact, the ram car moves in the original direction of v_0. Thus there exists a critical v_0 that can lead to puncture of the tank head and a motionless ram car after impact (or v=0). This critical v_0 is then the puncture velocity $v_{\mathrm{p,FE}} = v_{\mathrm{p0}}$ for the model problem and may be determined by assuming that all initial kinetic energy is consumed in initiating puncture:

$$\left[W_{\mathrm{ram}}/(2g)\right]v_{\mathrm{p0}}^2 = E_{\mathrm{p,FE}} \tag{8}$$

where W_{ram} is the weight of the ram car and g is the gravitational acceleration. The puncture velocity v_{p0} is then solved as

$$v_{\mathrm{p0}} = \sqrt{2gE_{\mathrm{p,FE}}/W_{\mathrm{ram}}} \tag{9}$$

More generally, the struck tank car assembly, which is stationary before impact, is assumed to gain an average velocity V after impact. The tank (W_{tank}) and backup car weights (W_{backup}) must now be considered and their combined weight W_{struck} is

$$W_{\mathrm{struck}}=W_{\mathrm{tank}}+W_{\mathrm{backup}} \tag{10}$$

Assuming that the initial kinetic energy is conserved except for those consumed in initiating puncture, and that momentum is conserved in the impact direction, we have

$$[W_{\mathrm{ram}}/(2g)]v_0^2=[W_{\mathrm{ram}}/(2g)]v^2+[W_{\mathrm{struck}}/(2g)]V^2+E_{\mathrm{p,\,FE}} \tag{11}$$

$$(W_{\mathrm{ram}}/g)v_0=(W_{\mathrm{ram}}/g)v+(W_{\mathrm{struck}}/g)V \tag{12}$$

As discussed in the model problem case, for puncture to be initiated, the ram and struck cars ought to move at the same speed in the same direction after impact

$$v=V \tag{13}$$

Solving Equations (11-13) yields the estimated puncture velocity

$$v_{\mathrm{p,FE}}=v_0|_{v=V}=\sqrt{2gE_{\mathrm{p,\,FE}}\left(1/W_{\mathrm{struck}}+1/W_{\mathrm{ram}}\right)} \tag{14}$$

In the model problem case, the boundary condition is equivalent to setting $W_{\mathrm{struck}}=\infty$ and consequently Equation (14) is reduced to Equation (9). If we further assume that the weight ratio between the ram and struck assemblies is

$$p=W_{\mathrm{struck}}/W_{\mathrm{ram}} \tag{15}$$

then $v_{\mathrm{p,FE}}$ can be expressed in terms of v_{p0} as

$$v_{\mathrm{p,FE}}=v_{\mathrm{p0}}\sqrt{1+1/p} \tag{16}$$

4. Puncture resistance case studies

Case studies were conducted again to apply the puncture analysis framework outlined above for the model problem (based on Case No. 5) as well as Case No. 2 of Table 1.

4.1 Model problem or Case No. 5

First, the equivalent plastic strain ($\bar{\varepsilon}^{\mathrm{pl}}$) contour was examined for the model problem with the moderate impact velocity v_0=8.5 mph and within the elastic-plastic framework using the ABAQUS shell element formulation. The $\bar{\varepsilon}^{\mathrm{pl}}$ distribution and the magnitude and location of the maximum $\bar{\varepsilon}^{\mathrm{pl}}$ ($\bar{\varepsilon}^{\mathrm{pl}}_{\mathrm{max}}$) in the domain were examined along with their dependence on (1) characteristic element size a expressed as a fraction of t (a=1t, t/2, t/3, etc.), and (2) number of through-the-thickness integration points.

To study the mesh size dependence, the problem domain was partitioned and locally refined in the impact area as illustrated in Figure 12. Global mesh refinement was considered unnecessary. The $\bar{\varepsilon}^{\mathrm{pl}}$ contour results showed that for a=1t, t/2 and t/3, while the predictions of $\bar{\varepsilon}^{\mathrm{pl}}$ distribution and $\bar{\varepsilon}^{\mathrm{pl}}_{\mathrm{max}}$ location were pretty consistent, those of the magnitude of $\bar{\varepsilon}^{\mathrm{pl}}_{\mathrm{max}}$ varied considerably from below 0.2 to around 0.5. This indicated potential mesh sensitivity in predicting fracture initiation with a strain-based criterion.

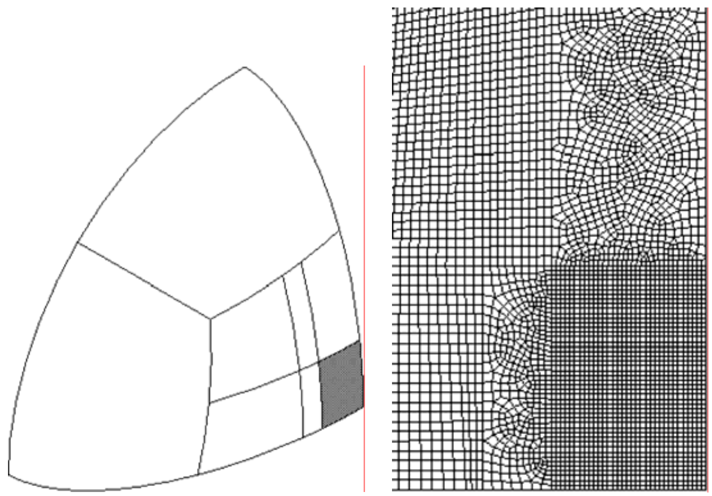

Figure 12. Local mesh refinement of the impact area in the model problem domain.

As to through-the-thickness integrations, ABAQUS allows 2-7 Gaussian points or at least 3 and only odd numbers of Simpson points (ABAQUS, 2006b). The $\bar{\varepsilon}^{\mathrm{pl}}$ contours with 5-7 Gaussian points and 15 Simpson points were compared. When Gauss quadrature was used, the $\bar{\varepsilon}^{\mathrm{pl}}$ distributions predicted by 5 and 7 points differed slightly from that predicted by 6 points. In the meantime, the $\bar{\varepsilon}^{\mathrm{pl}}$ distributions and $\bar{\varepsilon}^{\mathrm{pl}}_{\mathrm{max}}$ magnitudes predicted by 6 Gaussian points were fairly close to those by 15 Simpson points. As a result, we settled with 6 through-the-thickness Gaussian integration points in the puncture analyses.

Next, v_0 was increased to 16 mph to ensure that damage would occur in the dynamic simulations of the model problem. In addition, v_0= 20, 25 and 30 mph were simulated, and it appeared that the *F*-*d* responses corresponding to different v_0 were very comparable up to the peak forces, beyond which the softening responses were slightly prolonged with increased v_0. This indicated that the prediction of the puncture force would not differ much with a different impact velocity. Limited by available computational resources, only four levels of local mesh refinement were carried out with a=1t, t/2, t/3 and t/4, respectively. The fracture parameters for the M-115 steel calibrated in Section 3.2 were applied.

Figure 13(a) compares the *F*-*d* responses from the dynamic analyses with different local mesh refinement alongside the *F*-*d* curve obtained from the static analysis depicted in Figure 2. All *F*-*d* curves are indistinguishable up to a force level of nearly 300 kips, from which the dynamic curves start to become noisy and oscillate around the static curve. The maximum impact force $F_{\max}$ displays apparent mesh dependence, decreasing from 541.0 to 385.2 kips as a/t is reduced from 1 to 1/4. It appears that the true solution of $F_{\max}$ cannot be obtained except if a/t approaches zero. A regression analysis of $F_{\max}$ as a function of a/t were conducted as shown in Figure 13(b). The regression curve is linear with high correlation. The $F_{\max}$ with infinitesimal mesh refinement can be extrapolated from the regression curve and defined as the puncture force $F_{\mathrm{p,FE}}$

$$F_{\mathrm{p,FE}}=F_{\max}|_{a/t\to 0} \tag{17}$$

The puncture force $F_{\mathrm{p,FE}}$ was determined to be 329.6 kips in the model problem case.

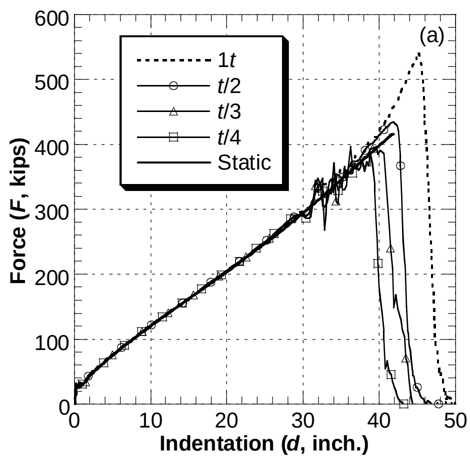

Figure 13. Puncture analyses for the model problem: (a) force-indentation (*F-d*) responses from dynamic analyses with an initial impact velocity v_0=16 mph and four levels of local mesh refinement as well as a static analysis, and (b) linear regression of the maximum force $F_{\max}$ as a function of *a/t* from the dynamic analyses.

Figure 14 shows the work-force or *W-F* plots translated from the *F-d* curves in Figure 13(a) by integration. The minimum energy required to puncture the tank head, $E_{\mathrm{p,FE}}$, was determined according to Equation (7) and identified as 5.913×10^6 lbf-inch. from the static *W-F* curve (most smooth among all curves). The point ($F_{\mathrm{p,FE}}$, $E_{\mathrm{p,FE}}$) is highlighted in Figure 14.

To estimate the puncture velocity $v_{\mathrm{p,FE}}$ for Case No. 5, the first attempt was to apply Equations (9) and (16) directly. However, there were three backup cars in this case and their weights were unknown. The dependence of $v_{\mathrm{p,FE}}$ on car weights was then studied for Case No. 5. The estimated $v_{\mathrm{p,FE}}$ is plotted against the struck to ram assembly weight ratio p in Figure 15. The curve corresponding to W_{ram}=128.9 kips is designated as the baseline, and W_{ram} is also varied relative to the baseline weight by -50%, -25%, +25% and +50%. The dependence of $v_{\mathrm{p,FE}}$ on both p and W_{ram} can then be implied from these curves.

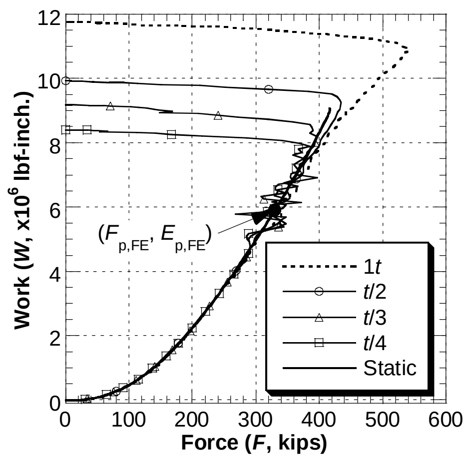

Figure 14. Dynamic and static work-force (*W-F*) plots translated from the *F-d* curves in Figure 13(a) by integration.

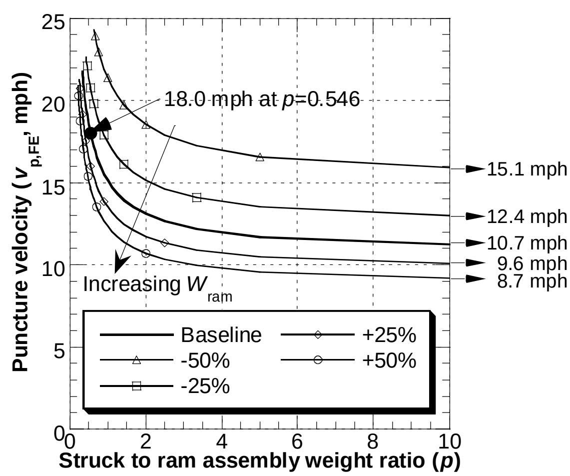

Figure 15. Estimated puncture velocity $v_{p,FE}$ as a function of the struck to ram assembly weight ratio (*p*) for Case No. 5 with different ram car weight W_{ram}.

Apparently $v_{p,FE}$ decreases as p increases with given W_{ram}, indicating that with more struck weights, there is less kinetic energy gained by the struck assembly, more energy concentration on initiating puncture and consequently puncture is more likely to occur. With the baseline W_{ram}, the plot indicates that $v_{p,FE}$ approaches v_{p0}=10.7 mph as p approaches infinity. According to Table 1, the puncture velocity estimated from the semi-empirical approach for Case No. 5 was $v_{p,SE}$=18.0 mph, which would correspond to p=0.546 on the baseline curve in Figure 15. In other words, the backup cars should weigh approximately W_{backup}=29.5 kips in total for Equations (9) and (16) to predict a $v_{p,FE}$ exactly as $v_{p,SE}$. This weight prediction appeared to be on the low side but could not be assessed otherwise because of unknown test setup.

As W_{ram} increases, the $v_{p,FE}$-p curves shift downwards and v_{p0} decreases, meaning with increased ram weight, lower impact velocity is needed to cause puncture. It also appears that v_{p0} becomes less sensitive to the changes in W_{ram} as W_{ram} increases. Such plots as those in Figure 15 can help to interpret an estimated puncture velocity within the context of the struck and ram assembly weights involved.

In summary, an estimate of $v_{p,FE}$ could not be given for Case No. 5 because of a lack of the W_{backup} data, but key results from the FEA analyses are still compared in Table 5 with those from the semi-empirical study. There appears to be an acceptable 14.0% difference in F_p predicted from the two approaches. Two additional quantities can be obtained from FEA: puncture energy E_p and puncture velocity v_{p0} with infinite struck weight. As the minimum energy required to puncture a tank head, E_p is a potentially important parameter in puncture resistance studies. As to v_{p0}, it represents the limit case where all the input kinetic energy is consumed in initiating puncture, so it depends only on E_p and the ram car weight W_{ram}. On the other hand, the puncture velocity v_p in a more general sense also depends on the weight of the struck assembly.

Table 2. Puncture analysis results for the model problem based on Case No. 5.

Quantity	Semi-empirical prediction	FEA prediction	Difference
F_{max} (kips)	-	$210.8a/t$+329.6 (R^2=0.999)	-
F_p (kips)	383.2	329.6	-14.0%
E_p (lbf-inch.)	-	5.913×10^6	-
v_{p0} (mph)	-	10.7	-
v_p (mph)	18.0	-	-

4.2 Case No. 2

The simulation setup for the puncture analyses of Case No. 2 was similar to that for the elastic-plastic analyses in Section 2.3. The initial impact velocity was v_0=30 mph. There were no backup cars, and the weight ratio calculated from the test data in Table 1 was p=0.376 (or 0.378 from model setup). A three-step approach was carried out and summarized as follows.

Step 1. Estimation of $F_{p,FE}$:

Step 1.1 Static analysis of a half tank car head with traction loads over a half circular area 1/3 down from the head center, and extraction of the F-d curve. The result is the static curve in Figure 16(a).

Step 1.2 Development of a half symmetry model for Case No. 2, dynamic analyses on four levels of mesh refinement (a=1t, t/2, t/3 and t/4, respectively) and extraction of the F-d curves. The results are the dynamic curves in Figure 16(a).

Step 1.3 Determination of the maximum forces F_{max} from the dynamic analyses, regression of the four data points (F_{max} vs. a/t) and determination of $F_{p,FE}$ as $F_{max}|_{a/t \to 0}$. The result is the linear regression shown in Figure 16(b).

Step 2. Estimation of $E_{p,FE}$:

Step 2.1 Calculation of the work W from the F-d curves (both static and dynamic) and plotting of the W-F curves.

Step 2.2 Identification of $E_{p,FE}$ on the static W-F curve according to Equation (7).

Step 3. Calculation of v_{p0} and $v_{p,FE}$ according to Equations (9) and (16).

The main results from the analyses of Case No. 2 are summarized in Table 3. Compared to the available semi-empirical data, the FEA prediction of the puncture force is about 12.5% lower, whereas that of the puncture velocity is about 9.0% higher.

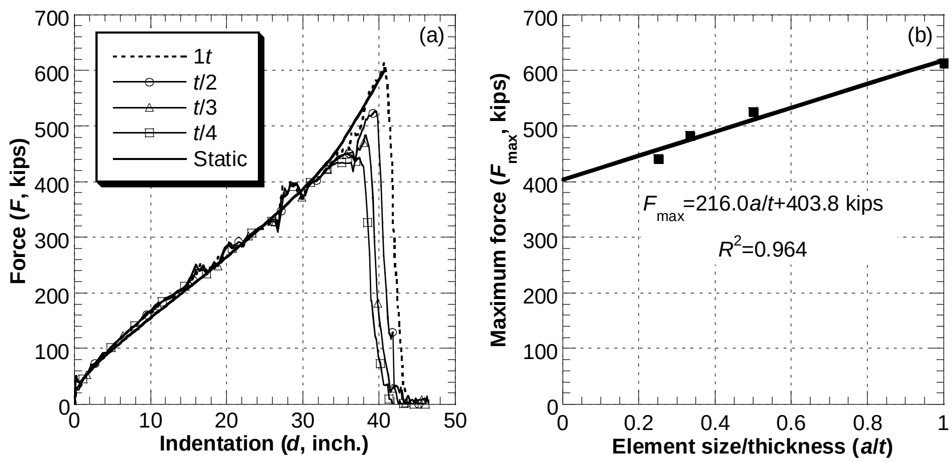

Figure 16. Puncture analyses for Case No. 2: (a) force-indentation (*F-d*) responses from dynamic analyses with an initial impact velocity v_0=30 mph and four levels of local mesh refinement as well as a static analysis, and (b) linear regression of F_{max} as a function of *a/t* from the dynamic analyses.

Table 3. Puncture analysis results for Case No. 2.

Quantity	Semi-empirical prediction	FEA prediction	Difference
F_{max} (kips)	-	$216.0a/t$+403.8 (R^2=0.964)	-
F_p (kips)	461.6	403.8	-12.5%
E_p (lbf-inch.)	-	6.789×10^6	-
v_{p0} (mph)	-	11.5	-
v_p (mph)	20.1	21.9	9.0%

5. Discussion

The fracture initiation criterion calibrated according to the Bao-Wierzbicki model has the underlying concept of averaged stress triaxiality over the plastic deformation history, but the "instantaneous" stress triaxiality is more likely employed by ABAQUS/Explicit to predict the onset of damage. Thus the fracture criterion needs to be reexamined within this context.

The analyses show that it is the strain concentration resulting from impact that ultimately causes a tank head to fracture. This combined with the strain-based fracture model leads to mesh dependence in predicting the puncture force. Automatic adaptive re-meshing technique with which a local mesh having high strain gradients is automatically refined can help to capture this strain concentration more efficiently.

The failure FEA in this study employed the shell element type as did the elastic-plastic FEA. Ongoing simulations intend to model the local impact zone with multiple layers of solid elements, whereas the non-impact zone remains to be modeled with shell elements via shell-to-solid coupling. This can gauge the sensitivity of a failure analysis to element types. The results of such analyses are forthcoming.

The prediction of v_{p0} and $v_{p,FE}$ is based on classical mechanical principles assuming that all kinetic energy is conserved except for that dissipated in plastic deformation, damage and friction leading directly to puncture, and that momentum is conserved. These assumptions are applied in the impact direction because the quantities in other directions are considered negligible. The accuracy of v_{p0} and $v_{p,FE}$ is then partially dependent on the validity of these assumptions.

The FEA framework presented in this paper can be further validated with more test cases. In addition, future work will incorporate fluids in a tank car, and side impacts without or with fluids will be considered as well. Tank car side impact is inherently different from head impact, but the same methodology is generally applicable. The inclusion of fluids, however, will probably call for additional analysis types or techniques, and the consideration of energy/momentum conservation will certainly need to include the more dynamic fluids.

6. Conclusions

In elastic-plastic FEA of tank car heads, both shell and solid element types are acceptable for static analyses, though the shell element type converges faster (3-4 through-the-thickness integration points and a=1t) than the solid element type (a=0.5t). In addition, in dynamic analyses, the shell element formulation in ABAQUS/Explicit predicts responses more agreeable with the static results than the solid element formulation does. Nevertheless, the differences in F_{max}, d_{max} and d_{res} from both element types are within 4%. The spatial convergence characteristics in dynamic analyses are similar to those in static analyses, i.e., 3-4 through-the-thickness integration points and a=1t or 2t. The predicted impact forces and indentations in two test cases are within acceptable ranges of the test data and the results from an alternative semi-empirical method.

A failure FEA framework was further outlined to predict the puncture resistance of a tank car head in impact. The framework can be applied to predict puncture force ($F_{p,FE}$), puncture energy ($E_{p,FE}$), puncture velocity with infinite struck weight (v_{p0}) and puncture velocity ($v_{p,FE}$) in a tank car head impact event. The prediction of $F_{p,FE}$ for Case No. 5 is 14.0% lower than the semi-empirical prediction $F_{p,SE}$, whereas $F_{p,FE}$ for Case No. 2 is 12.5% lower than $F_{p,SE}$. The prediction of $v_{p,FE}$ for Case No. 2 is 9.0% higher than $v_{p,SE}$. The $v_{p,FE}$ for Case No. 5 could not be predicted because of unknown backup car weight W_{backup}, but an estimation of W_{backup} was made based on $v_{p,SE}$ for this case. The estimated W_{backup} appears to be on the low side but could not be assessed otherwise. Judged from both $E_{p,FE}$ and v_{p0}, the tank car head in Case No. 2 appears to be more puncture resistant than that in Case No. 5.

7. Acknowledgement

The work presented in this paper was sponsored by Office of Research & Development, the Federal Railroad Administration. Ms. Claire Orth is the Chief of the Equipment and Operating Practices Division. Mr. Francisco Gonzalez is the project manager for research on railroad tank cars. Technical discussion with Dr. Oscar Orringer and Mr. Jeff Gordon of the Volpe Center and Professor Benjamin Perlman of Tufts University is gratefully acknowledged.

8. References

1. ABAQUS Inc., ABAQUS Analysis User's Manual, Version 6.6, 2006a.
2. ABAQUS Inc., ABAQUS Keywords Reference Manual, Version 6.6, 2006b.
3. Bao, Y., Prediction of Ductile Crack Formation in Uncracked Bodies, Ph.D. Thesis, Massachusetts Institute of Technology, September 2003.
4. Coltman, M., and M. Hazel, "Chlorine Tank Car Puncture Resistance Evaluation," Final Report, DOT/FRA/ORD-92/11, 1992.
5. Comi, C., "A Non-Local Model with Tension and Compression Damage Mechanisms," Eur. J. Mech. A/Solids, 20:1–22, 2001.
6. Hicho, G.E., and D.E. Harne, "Mechanical Properties and Fracture Toughness of AAR TC-128B Steel in the Normalized, and Normalized and Stress Relieved Conditions," NISTIR 4660, Report No. 24, National Institute of Standards and Technology, September 1991.
7. Hooputra, H., H. Gese, H. Dell, and H. Werner, "A Comprehensive Failure Model for Crashworthiness Simulation of Aluminium Extrusions," International Journal of Crashworthiness, Vol. 9, No. 5, pp. 449–463, 2004.
8. Jeong, D.Y., Y.H. Tang, and A.B. Perlman, "Evaluation of Semi-Empirical Analyses for Railroad Tank Car Puncture Velocity, Part I: Correlations with Experimental Data," Final Report, DOT/FRA/ORD-01/21.I., 2001a.
9. Jeong, D.Y., Y.H. Tang, and A.B. Perlman, "Evaluation of Semi-Empirical Analyses for Railroad Tank Car Puncture Velocity, Part II: Correlations with Engineering Analyses," Final Report, DOT/FRA/ORD-01/21.II., 2001b.
10. Jeong, D.Y., Y.H. Tang, H. Yu, and A.B. Perlman, "Engineering Analyses for Railroad Tank Car Head Puncture Resistance," Proceedings of IMECE2006, 2006 ASME International

Mechanical Engineering Congress and Exposition, Chicago, Illinois, USA, November 5-10, 2006.

11. Larson, W.G., “Aluminum/Cold Temperature Tank Car Puncture Resistance Tests: Data Report,” Final Report, DOT/FRA/ORD-92/29, 1992.
12. Lee, Y.-W., and T. Wierzbicki, “Quick Fracture Calibration for Industrial Use,” Impact & Crashworthiness Laboratory, Massachusetts Institute of Technology, Report No: 115, August 2004.
13. Livermore Software Technology Corporation (LSTC), LS-Dyna Keyword User’s Manual, Version 970, April 2003.
14. National Transportation Safety Board (NTSB), “Derailment of Canadian Pacific Railway Freight Train 292-16 and Subsequent Release of Anhydrous Ammonia Near Minot, North Dakota January 18, 2002,” Railroad Accident Report NTSB/RAR-04/01, March 2004.
15. National Transportation Safety Board (NTSB), “Collision of Norfolk Southern Freight Train 192 With Standing Norfolk Southern Local Train P22 With Subsequent Hazardous Materials Release at Graniteville, South Carolina January 6, 2005,” Railroad Accident Report NTSB/RAR-05/04, November 2005.
16. National Transportation Safety Board (NTSB), “Collision of Union Pacific Railroad Train MHOTU-23 With BNSF Railway Company Train MEAP-TUL-126-D With Subsequent Derailment and Hazardous Materials Release, Macdona, Texas, June 28, 2004,” Railroad Accident Report NTSB/RAR-06/03, July 2006.
17. Phillips, E.A., and L. Olsen, “Final Phase 05 Report on Tank Car Head Study,” RPI-AAR Tank Car Safety Research and Test Project, Report RA-05-1-17, 1972.
18. Pijaudier-Cabot, G., and Z.P. Bazant, “Nonlocal Damage Theory,” Journal of Engineering Mechanics. Vol. 113, No. 10, pp. 1512-1533, 1987.
19. Stahl, S.W., “Puncture Resistance of Non-Pressure Tank Cars,” HLA Report No. 99320-0, HLA Engineers, Inc., June 2000.
20. Wierzbicki, T., Y. Bao, Y.-W. Lee, and Y. Bai, “Calibration and Evaluation of Seven Fracture Models,” International Journal of Mechanical Sciences, Vol. 47, pp.719-743, 2005.
21. Zahoor, A., “Materials and Fracture Mechanics Assessments of Railroad Tank Cars,” NISTIR 6266, National Institute of Standards and Technology, September 1998.